

Automatic centroid detection and surface measurement with a digital Shack–Hartmann wavefront sensor

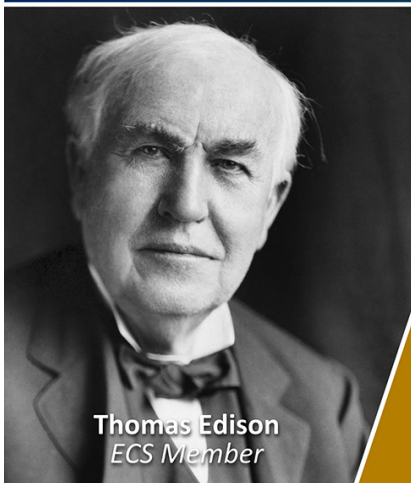
To cite this article: Xiaoming Yin *et al* 2010 *Meas. Sci. Technol.* **21** 015304

View the [article online](#) for updates and enhancements.

You may also like

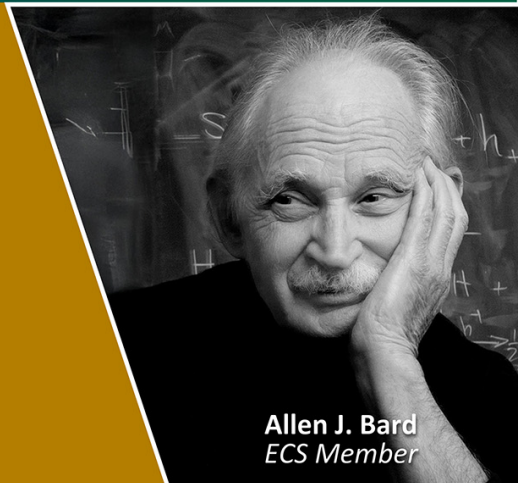
- [Micro-Alvarez lenses for a tunable-dynamic-range Shack–Hartmann wavefront sensor](#)
Eva Acosta and Jose Sasian
- [High-precision Shack-Hartmann wavefront sensing with a multi-focal diffraction Taiji-lenslet array](#)
Yaling Yang, Yanli Zhang, Junyong Zhang et al.
- [The rapid rise of severe marine heat wave systems](#)
J Xavier Prochaska, Claudie Beaulieu and Katerina Giannalaki

Join the Society Led by Scientists, for *Scientists Like You!*



Thomas Edison
ECS Member

ECS
The
Electrochemical
Society
Advancing solid state &
electrochemical science & technology



Allen J. Bard
ECS Member

Automatic centroid detection and surface measurement with a digital Shack–Hartmann wavefront sensor

Xiaoming Yin, Liping Zhao, Xiang Li and Zhongping Fang

Singapore Institute of Manufacturing Technology, 71 Nanyang Drive, Singapore 638075

E-mail: xmyin@SIMTech.a-star.edu.sg

Received 9 June 2009, in final form 5 November 2009

Published 7 December 2009

Online at stacks.iop.org/MST/21/015304

Abstract

With the breakthrough of manufacturing technologies, the measurement of surface profiles is becoming a big issue. A Shack–Hartmann wavefront sensor (SHWS) provides a promising technology for non-contact surface measurement with a number of advantages over interferometry. The SHWS splits the incident wavefront into many subsections and transfers the distorted wavefront detection into the centroid measurement. So the accuracy of the centroid measurement determines the accuracy of the SHWS. In this paper, we have presented a new centroid measurement algorithm based on an adaptive thresholding and dynamic windowing method by utilizing image-processing techniques. Based on this centroid detection method, we have developed a digital SHWS system which can automatically detect centroids of focal spots, reconstruct the wavefront and measure the 3D profile of the surface. The system has been tested with various simulated and real surfaces such as flat surfaces, spherical and aspherical surfaces as well as deformable surfaces. The experimental results demonstrate that the system has good accuracy, repeatability and immunity to optical misalignment. The system is also suitable for on-line applications of surface measurement.

Keywords: digital Shack–Hartmann wavefront sensor, centroid detection, surface measurement, on-line inspection

(Some figures in this article are in colour only in the electronic version)

1. Introduction

With the breakthrough of manufacturing technologies, workpieces with pre-defined profiles can be fabricated with high throughput. The measurement of surface profiles becomes a big issue. Surface measurement systems face more challenges than before, for example:

- Measurement capability of large flat surfaces, e.g. guide, glass panel, etc [1]
- Measurement capability of surfaces with pre-defined profiles, such as aspherical, toroidal surfaces, etc [2]
- Dynamic measurement of part deformation. Warpage/deformation occurs in thin flat panels, and needs to be inspected in real time in some applications
- High throughput with sufficient accuracy for on-line measurement. Some of the parts need to be 100% measured in the production line for quality control

- Parallel measurement in the whole area without scanning mechanism
- Insensitivity to vibration. The measurement needs to be conducted in industrial environment, and the measurement system needs to be insensitive to vibration and noise
- Easy operation. The loading/unloading of objects needs to be convenient, and the alignment of the measurement system needs to be easy
- System flexibility. The system can be easily re-configured with different fields of measurement for various workpieces in different dimensions
- Cost efficiency.

A commonly used tool to measure the surface profile is a stylus instrument [3]. However, a non-contact measurement instrument is preferred to a contact instrument for most surface

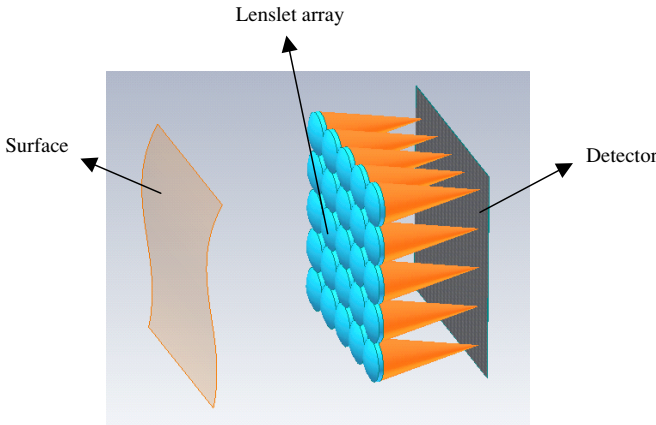


Figure 1. Surface profile measurement by a Shack–Hartmann wavefront sensor (this figure is reproduced from [11]).

measurement applications. Various interferometric techniques have been used for non-contact surface measurement, including fringes of equal chromatic order (FECO) [4], Nomarksi polarization interferometry [5], Tolansky multiple-beam interferometry and two-beam interferometry based on Michelson, Linnik and Mirau [6, 7]. In these methods, two-beam interferometry with phase-shifting technology is mostly used. However, phase-shifting technology is especially susceptible to vibration and turbulence within the testing environment, making it less suitable for large-optic or on-line applications.

A wavefront is the locus of points that have the same phase, i.e. the same optical path lengths (OPL) from a light source. When a wavefront is reflected by a surface, it will carry the information of the surface topography. The imprint information of the surface can be extracted by the measurement and analysis of the wavefront.

A Shack–Hartmann wavefront sensor (SHWS) samples the incident wavefront by means of a lenslet array which produces an array of spots on a detector such as a CCD camera, as shown in figure 1. Basically, SHWS is a comparison method where the output of the measurement is the difference between the target surface and the reference surface. The reference wavefront is reflected from a standard surface, such as a flat surface or a spherical surface, and the measurement wavefront is reflected from a target surface. The reference wavefront produces a regular array of focal spots on the detector, and the measurement wavefront produces a distorted spot pattern. When these two spot patterns are compared, a map of the wavefront slopes is produced. And integration of these slopes allows reconstruction of the measurement wavefront.

The SHWS provides an alternative technology for non-contact surface measurement. It offers a number of advantages over interferometry for large-optic metrology applications, according to some researchers' comparative studies [8, 9]. These advantages include a large dynamic range, immunity to optical misalignment, insensitivity to vibration and noise, less complex and less expensive.

These advantages make the SHWS a promising technology for surface measurement. It could meet most of the challenges faced by the surface measurement system.

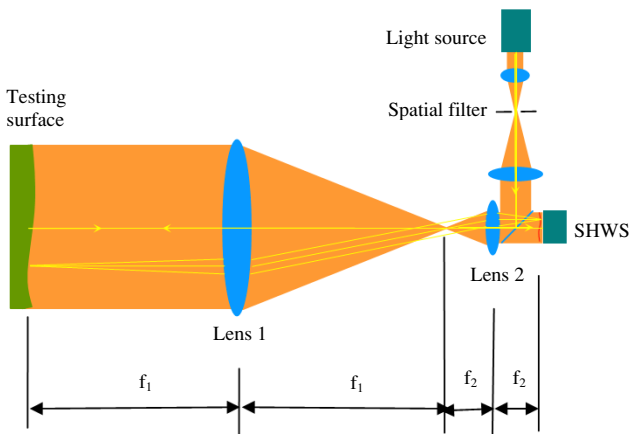


Figure 2. Optical setup of a SHWS for surface profile measurement.

Especially, it is very suitable for on-line applications. However, the advantages of the SHWS are balanced by heavy reliance on the fidelity of the centroid detection algorithm and by the trade-off between spatial resolution and wavefront sensitivity related to the choice of lenslet diameter, spacing and focal length [10].

In this paper, we have presented a new centroid detection algorithm, and built a digital SHWS system which has been used for surface measurement. The presented centroid detection algorithm can automatically detect the centroid of each focal spot using an adaptive threshold in a dynamically identified detection window by utilizing image-processing techniques. Based on this automatic centroid detection method, we have developed a digital SHWS system which can measure the surface profile automatically. The focal length, size, pitch, format and layout of the lenslet array of the digital SHWS can be changed flexibly according to requirements of different applications. The system has been tested using various simulated and real surfaces such as plate surfaces, spherical and aspherical surfaces as well as deformable surfaces.

The rest of the paper is organized as follows. We first give the schematic diagram of the optical setup and introduce the digital SHWS in section 2. The proposed automatic centroid detection method is presented in section 3. In section 4, we talk about wavefront reconstruction. Then we study the accuracy and repeatability of the system as well as the influence of misalignment on the system by experiments in sections 5, 6 and 7. Some measurement results of real surfaces such as aspherical and deformable surfaces are given in section 8. Lastly, the conclusion is drawn in section 9.

2. Optical setup

2.1. Optical system for surface measurement

Figure 2 shows the schematic diagram of the optical setup for surface measurement. It is a $2f+2f$ system in which two lenses are employed. The back focal point of lens 1 coincides with the front focal point of lens 2. The testing surface is placed on the front focal plane of lens 1, and the SHWS is placed on the back focal plane of lens 2.

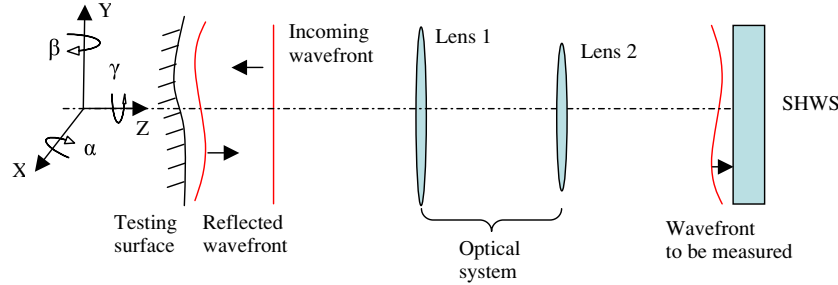


Figure 3. Wavefront propagation in the $2f+2f$ optical system for surface profile measurement.

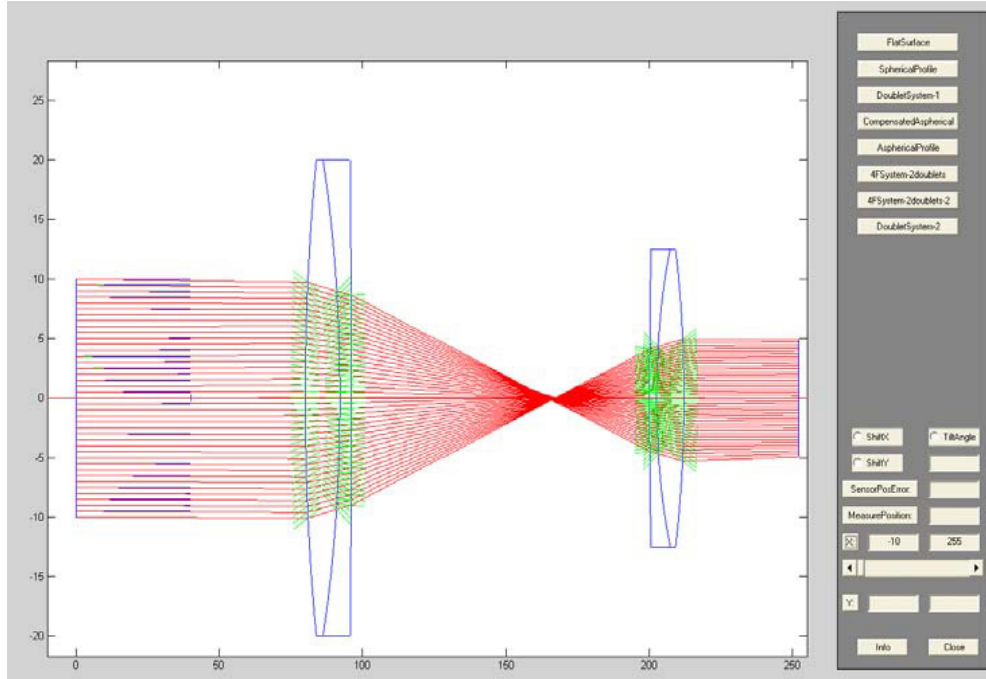


Figure 4. Wavefront propagation simulated by our wavefront tracing platform (this figure is reproduced from [11]).

In order to investigate the relationship between the surface profile and the wavefront, we have developed a software platform to simulate the propagation of wavefront in the optical system with the combination of ray tracing and phase tracing. Figure 3 shows the schematic concept of the platform design. A standard wavefront strikes a surface and is reflected by the surface. Then it passes through the optical system and enters the SHWS. The platform can simulate the wavefront profile in every position of the system.

Figure 4 shows the propagation of a wavefront in a $2f+2f$ optical system simulated by the platform. The testing surface is a polynomial curve generated by the software. All the lenses use commercially available parts, and all the parameters are those of real parts. The wavelength is $0.6328 \mu\text{m}$. Figure 5 shows the output wavefront simulated by the platform, $W_{\text{output}} = W_{\text{meas}} - W_{\text{ref}}$. Here a super-plane surface is used as the reference. The envelope of W_{output} is $7.636 \mu\text{m}$, and the envelope of P_{surface} is $3.8 \mu\text{m}$. The output wavefront approximates two times the surface profile. A more detailed description of the wavefront simulation can be found in [11].

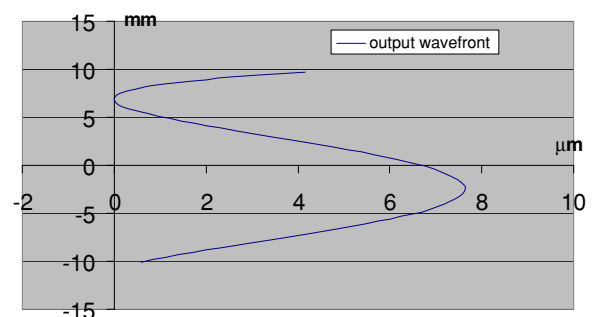


Figure 5. Output wavefront of the SHWS simulated by the wavefront tracing platform (this figure is reproduced from [11]).

2.2. Digital Shack–Hartmann wavefront sensor

We have built a digital Shack–Hartmann wavefront sensor in which a spatial light modulator (SLM) is employed to replace the physical lenslet array used in a conventional SHWS. A SLM consists of an array of optical elements or pixels where each pixel can modulate the amplitude and phase of the

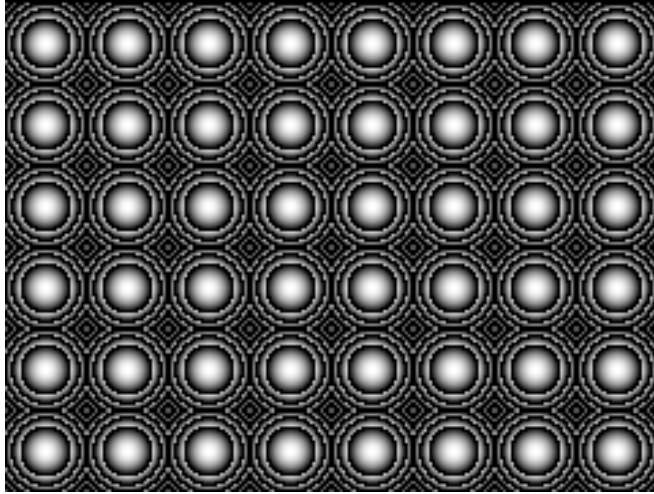


Figure 6. Lenslet array generated with a spatial light modulator.

incident light. So the lenslet of the digital SHWS can be formed by the programming of pixels of the SLM based on the technique of diffractive optics element (DOE), which has been presented in [12]. The focal length, size, pitch, format and layout of the lenslet array can be changed according to requirements of different applications. The dynamic range and accuracy of the digital SHWS will change accordingly and the adaptive measurement can be realized.

Figure 6 shows a lenslet array generated with a SLM, and figure 7 shows the array of focal spots detected by a CCD camera. In this image, an 8×6 lenslet array is generated with the SLM. The focal length of the lenslet is 60 mm, and the wavelength is 633 nm. The pixel size of the SLM is $32 \mu\text{m}$, the spacing between the lenslet is 30 pixels or $960 \mu\text{m}$ and the radius of the lenslet is 15 pixels or $480 \mu\text{m}$. Diffractive optical lenslets are uniformly distributed and the diameters of the lenslets are also the same. The resolution of the CCD is 768×572 , and the pixel size is $8 \mu\text{m}$.

The diffractive lenslet array generated with the SLM functions well in the wavefront sensing system with greater flexibility and programmability compared with the traditional physical lenslet array. However, besides the focal spots, there are some bright spots observed on the focal plane as well, as shown in figure 7. These undesired spots are caused by the diffraction of the SLM's grating structure, since the screen of the SLM is actually a 2D grating with the pitch size equal to the pixel size of the SLM. The positions of these diffraction spots keep changing with the pixel size of the SLM, the focal length of the lenslet and the wavelength of the light source. Sometimes, these diffraction spots are even brighter than the focal spots. Moreover, these undesired diffraction spots cannot be eliminated practically due to the coherent light source used in our system.

3. Automatic centroid detection algorithm

3.1. Commonly used centroid detection algorithms

The SHWS spatially samples and focuses the incident wavefront by a lenslet array on a suitable detector such as

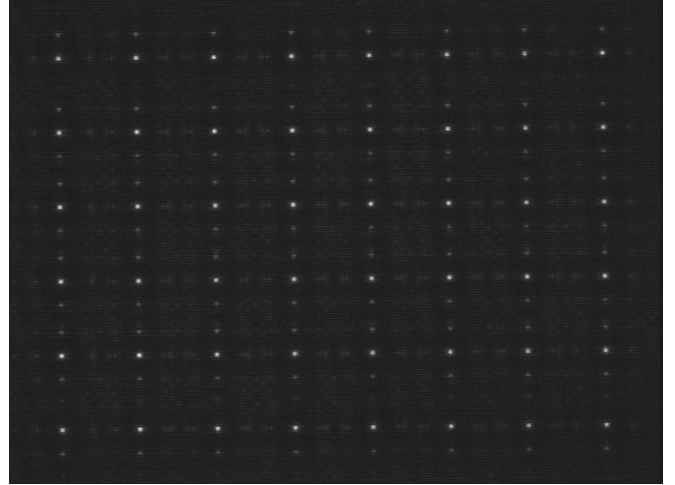


Figure 7. Focal spots array detected by a CCD camera.

a CCD camera. This provides an array of focus spots, each corresponding to a sub-aperture sampled datum. The accuracy of the SHWS is mainly dependent upon the measurement accuracy of the centroid of each spot [13–15]. Many methods have been presented to improve the accuracy of the centroid measurement [16–19]. The commonly used methods include statistic averaging, thresholding and windowing algorithms. The statistical averaging algorithm, i.e. the center of mass, is the most widely used method according to the definition of centroid. However, this method is sensitive to the influence of the noise, particularly in the case where the signal spot area is relatively small compared with the detection area. In the thresholding algorithm, a threshold is used to improve the signal to noise ratio (SNR). In the windowing algorithm, the detection window size is changed to reduce the influence of the noise. Based on these methods, other improved algorithms have also been proposed [20–22].

However, most centroid detection methods have been proposed and analyzed from the point of view of optics, based on the assumption that the intensity distribution of the spot image has a Gaussian pattern or an Airy disk pattern. In our work, we have applied a digital SHWS to the profile measurement of real surfaces. The spot image of the digital SHWS does not have a Gaussian pattern or Airy disk pattern any more due to the diffraction of the SLM's grating. The diffraction noise of the digital SHWS makes centroid detection more difficult and inaccurate if using common centroid detection algorithms. In order to eliminate the effect of diffraction noise, we propose the following centroid detection algorithm based on an adaptive thresholding and dynamic windowing method.

3.2. Determine sub-areas of focal spots

In most methods that have been presented, the centroid is measured for only one sub-aperture from the image which is generated by simulation or detected by a CCD camera. The detection area is usually set as the corresponding region of the sub-aperture on the CCD. However, we cannot consider only one sub-aperture in practical applications such as surface

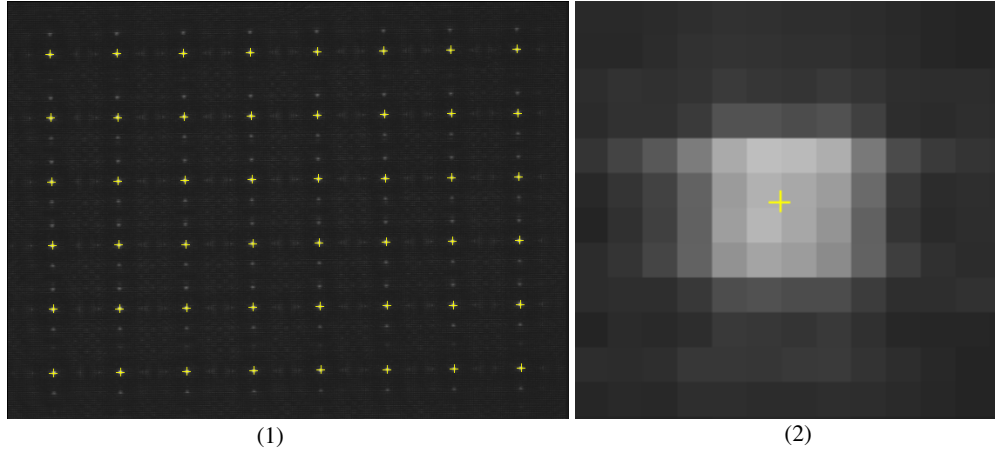


Figure 8. (1) Detected centroids by the auto-algorithm; (2) enlarged picture of one centroid.

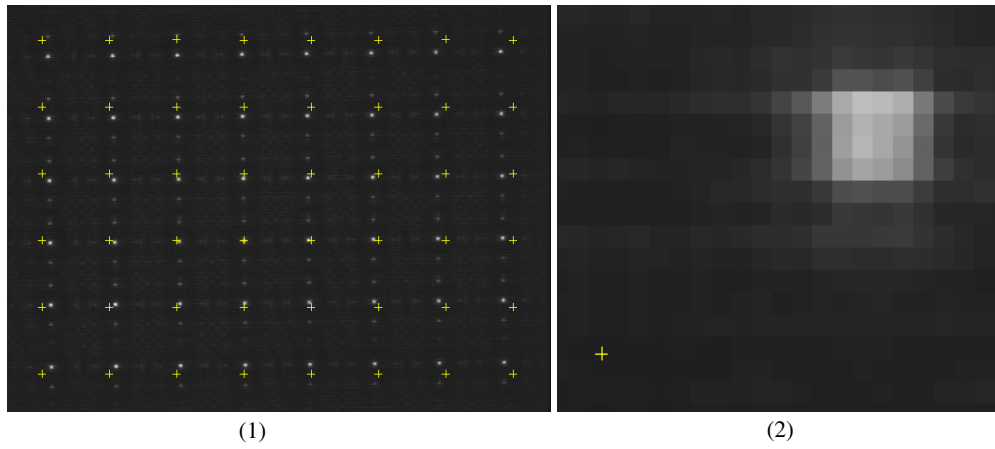


Figure 9. (1) Detected centroids by the averaging algorithm; (2) enlarged picture of one centroid.

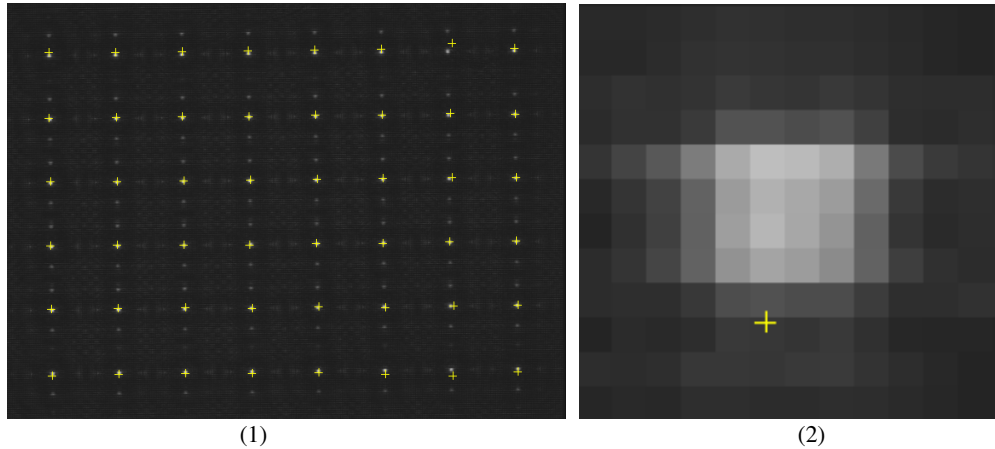


Figure 10. (1) Detected centroids by the thresholding algorithm; (2) enlarged picture of one centroid.

measurement. We also cannot get the detection area of each focal spot by just dividing the image uniformly based on the size and number of sub-apertures, because the CCD may not be big enough to cover all the sub-apertures, or there is a shift or tilt of positions of focal spots on the image.

In our method, we do not determine the detection area based on the exact dimension of the sub-aperture. Instead,

we determine the detection area of each focal spot directly on the image. Based on the positions of focal spots in the image, we first determine the sub-areas of focal spots, and then identify the detection area of each focal spot using the algorithms described in the following subsection. The size of the spot sub-area is defined manually without any strict limitation. The only requirement is that one sub-area should cover only one focal spot. So the sub-areas of focal spots are

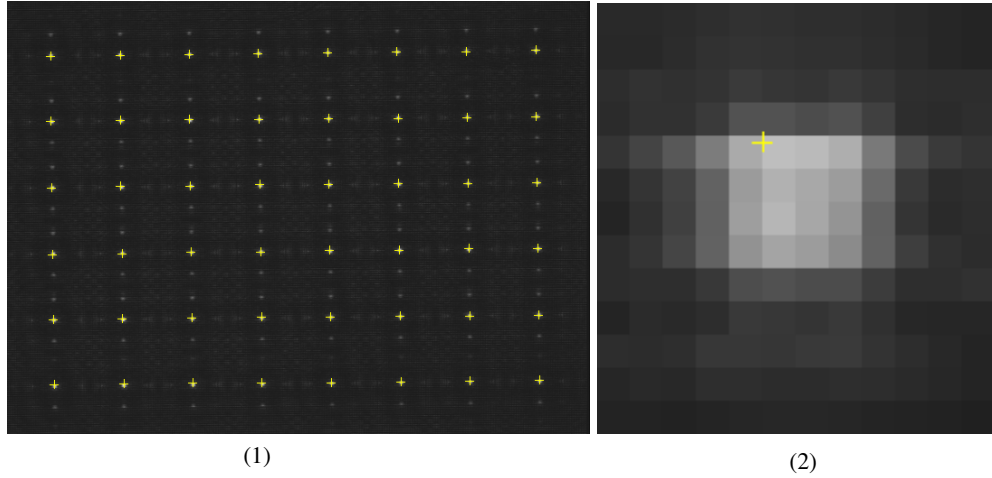


Figure 11. (1) Detected centroids by the windowing algorithm; (2) enlarged picture of one centroid.

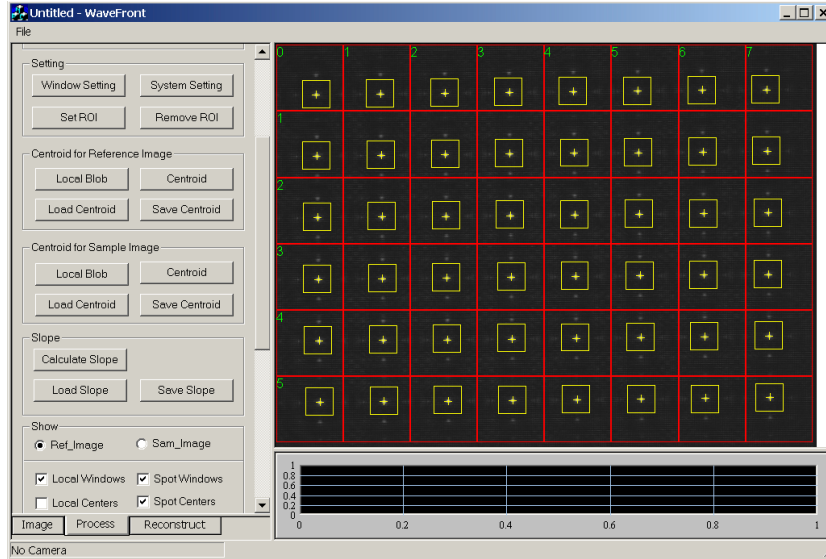


Figure 12. Interface of the developed automatic centroid detection software.

very easy to define in the image without knowing the physical properties of the lenslet array.

3.3. Detect focal spots

The position of the focal spot will strongly influence the accuracy of centroid calculation of common centroid detection algorithms such as statistic averaging and windowing algorithms. In the case where the centroid of the focal spot is not at the center of the detection area, these algorithms will result in a relatively high systemic error. Some algorithms locate the brightest pixel as the approximate center of the focal spot. But in the case of strong readout noise and weak signal, the brightest pixel may not be on the focal spot. When the focal spot is not detected, the centroid calculation with these methods is completely wrong.

In our method, we propose the following algorithm to detect focal spots.

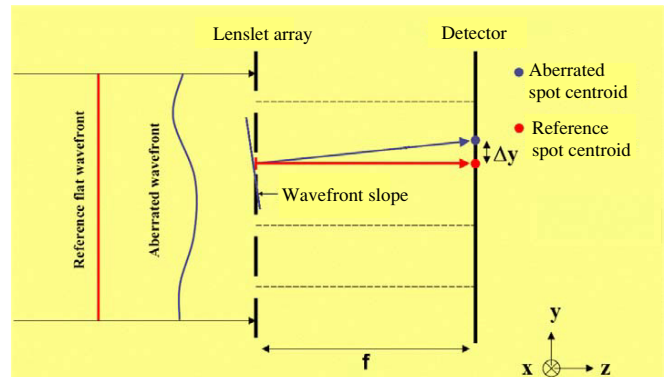


Figure 13. Calculation of the wavefront slope.

- (1) Find the n th high intensity value I_i^n in the sub-area of each focal spot.
- (2) Use I_i^n as the threshold to binarize the image in each focal spot sub-area and select the biggest blob in the binary image as the focal spot.

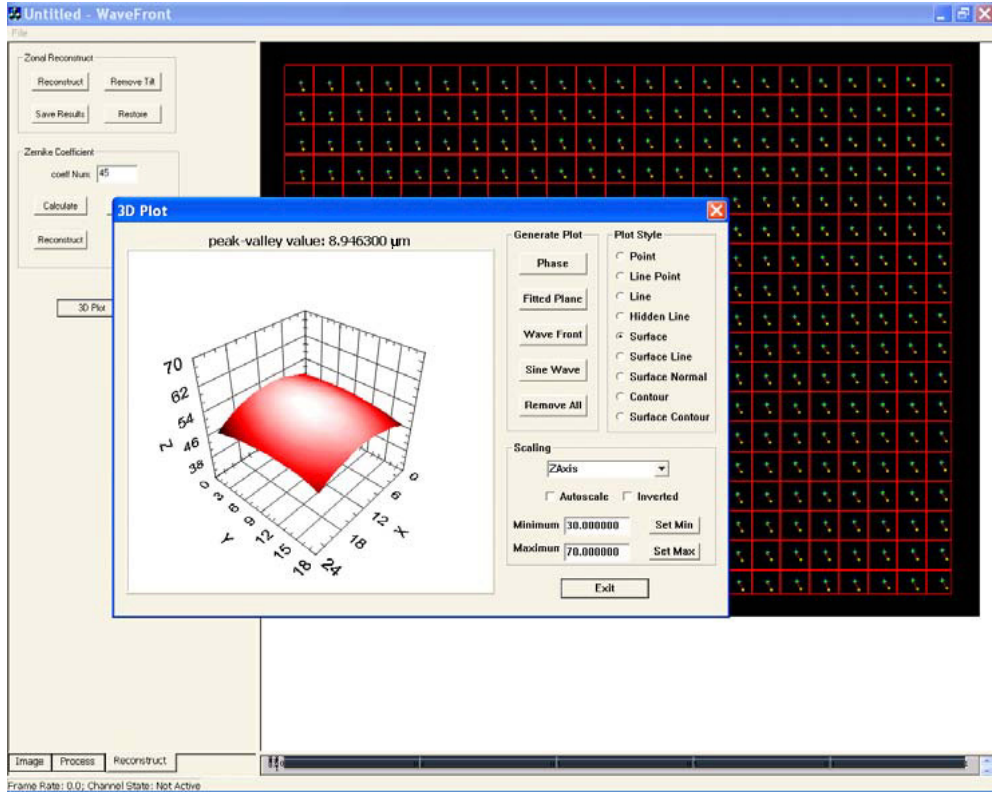


Figure 14. Interface of the developed automatic wavefront reconstruction software.

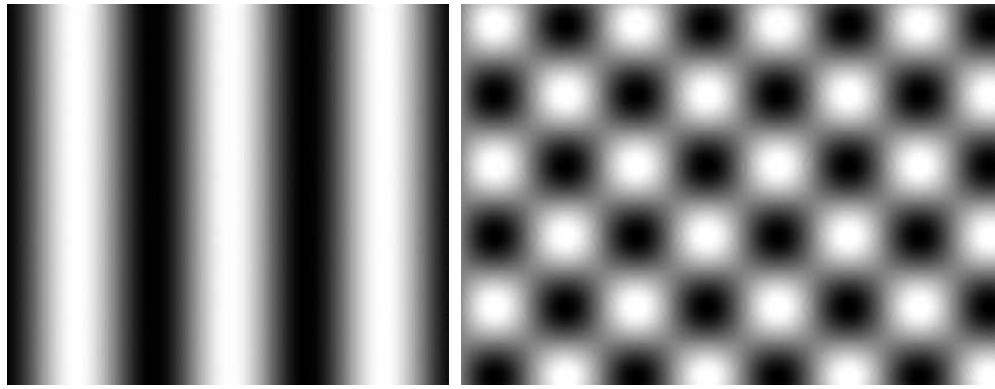


Figure 15. Sine wavefront patterns generated by the SLM.

- (3) Calculate the center of mass of the biggest blob C_i as the approximate center of the focal spot.

Here, we do not find the highest intensity value, but the n th high intensity value as the threshold. For example, the intensity value of a focal spot sub-area has the following distribution: 250, 248, 245, 230, 200, 150, 140.... If n is chosen as 4, the 4th high intensity value is 230. So the intensity value of 230 is determined as the threshold to binarize the image in this focal spot sub-area. We do not set the threshold to a direct intensity value, because the intensity distribution of each focal spot sub-area may be different due to the uneven light source. It is difficult to find a single intensity value which can segment every focal spot image well in the case that the intensity of the whole image is not uniform.

Then the biggest blob after binarization is determined as the focal spot, and the center of mass of this blob is calculated as the approximate center of the focal spot. By using this method, the influence of those noisy pixels, which have relative high intensity value but small area, is eliminated.

3.4. Calculate centroids

After the focal spots have been detected, the detection area of each focal spot centroid can be identified dynamically based on the focal spot center. The detection area is defined as a rectangular window surrounding a focal spot in the image, which is centered at the focal spot center. The size of the

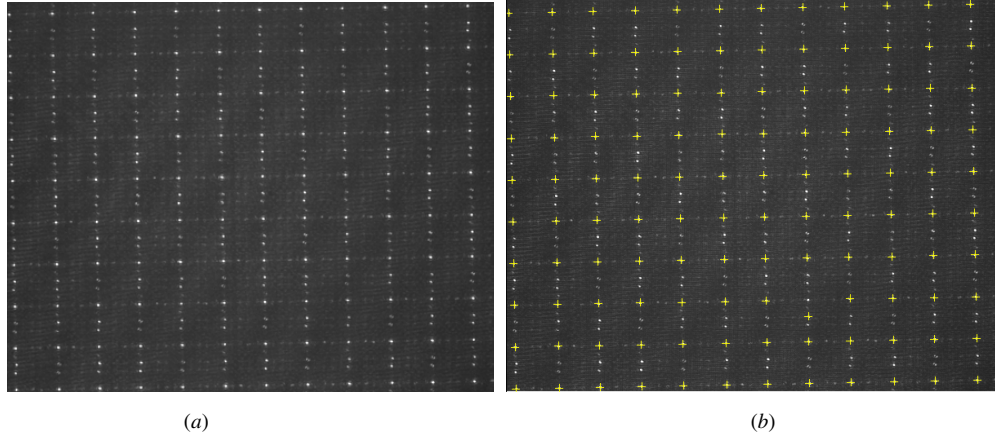


Figure 16. (a) Focal spot image generated by the digital SHWS; (b) detected centroids of focal spots.

window can be set manually according to the area of the focal spot.

After that, the centroid of each focal spot is calculated using the thresholding method from the pixels within the detection window. But the threshold is set the same as I^n , the n th high intensity value in the focal spot sub-area, which has been used as the threshold for focal spot detection in section 3.3. It is a threshold adaptive to the intensity distribution of each focal spot sub-area.

The calculation equations are as follows:

$$x_c = \frac{\sum_{i=1}^U \sum_{j=1}^V (I(i, j) - I^n) H(i, j) \cdot x_{ij}}{\sum_{i=1}^U \sum_{j=1}^V (I(i, j) - I^n) H(i, j)} \quad (1)$$

$$y_c = \frac{\sum_{i=1}^U \sum_{j=1}^V (I(i, j) - I^n) H(i, j) \cdot y_{ij}}{\sum_{i=1}^U \sum_{j=1}^V (I(i, j) - I^n) H(i, j)} \quad (2)$$

$$H(i, j) = \begin{cases} 1, & I(i, j) \geq I^n \\ 0, & I(i, j) < I^n \end{cases} \quad (3)$$

where x_c and y_c are the centroid positions of the focal spot. $I(i, j)$ is the intensity value of the (i, j) pixel. I^n is the n th high intensity value in this focal spot sub-area. x_{ij} and y_{ij} are the coordinates of the (i, j) pixel in the whole spot image. U and V are the numbers of the pixels along X and Y directions in the detection window, respectively.

Our method actually aligns the center of the detection area with the center of the focal spot by dynamically identifying the detection window of each focal spot based on the spot center. The method also detects the centroid of each focal spot using an adaptive threshold. By aligning the center of the detection area with the center of the focal spot, the influence of the noise on common windowing and thresholding algorithms is reduced, and the accuracy of the algorithm is improved greatly, even the focal spot locating far from the center of the spot sub-area. By dynamically setting the detection window and adaptively selecting the threshold of each focal spot, the influence of those noises such as diffraction of the digital SHWS, unevenness and instability of the light source is also reduced, and the centroid of each focal spot can be detected very precisely.

3.5. Algorithm performance

We compare our centroid detection algorithm, which is referred to the auto-centroid algorithm, with some other commonly used algorithms such as statistical averaging, thresholding and windowing algorithms. Figure 8(1) shows the centroids of focal spots detected by the auto-algorithm from the image shown in figure 7 and 8(2) shows the enlarged picture of one centroid. Figure 9(1) shows the detected centroids by the averaging algorithm from the same image shown in figure 7. Figure 9(2) shows the enlarged picture of one centroid for the same focal spot as shown in figure 8(2). Figure 10 shows the detected centroids by the thresholding algorithm and figure 11 shows the detected centroids by the windowing algorithm. It can be observed that the centroid detected by the auto-algorithm has the most precise position in the image.

We have also conducted stability and repeatability experiments using real waveform images, and compared the performances of these four algorithms. We captured 36 spot images using the digital SHWS within 6 h, one image per 10 min. The spot images were generated intentionally with a laser diode light source which is unstable and introduces a lot of noise into spot images. The mean and standard deviation of the centroids detected by four algorithms are calculated, respectively. Table 1 shows the calculation results for three centroids detected for three focal spots. The last two columns show the overall standard deviations of X and Y coordinates of centroids calculated from all the focal spots. The overall standard deviation of X coordinates detected by our algorithm is 0.078 pixel, or $0.624 \mu\text{m}$ since the pixel size of the CCD is $8 \mu\text{m}$. The overall standard deviation of Y coordinates is 0.027 pixel, or $0.216 \mu\text{m}$. They are much better than those detected by the other three algorithms.

In addition, our algorithm employs some image-processing techniques which are simple and easy to implement. So the processing speed of the algorithm is very fast. In our experiment, the whole process of an image with the resolution of 768×572 can be completed within 100 ms on a 3.20 GHz Pentium 4 PC.

A software system has been developed for automatic centroid detection. Figure 12 shows the interface of the

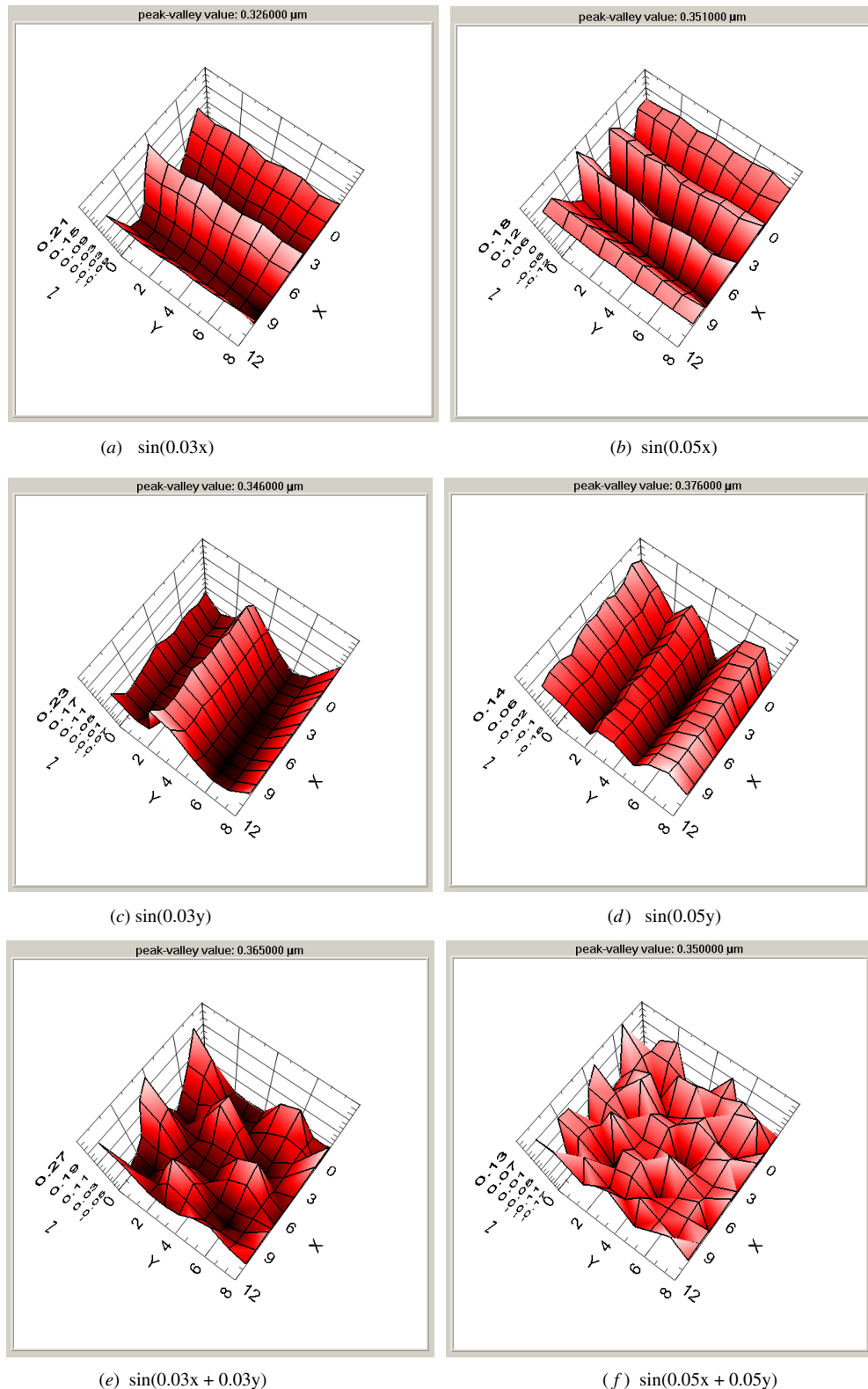


Figure 17. Profiles of the reconstructed sine wavefront.

software. The software can generate focal spot sub-areas, detect the centers of focal spots, identify the detection windows and calculate the centroids automatically. The only parameters that need to be input are the size of focal spot sub-areas, the position of the first focal spot sub-area, the intensity level of

threshold and the size of detection windows. The size of focal spot sub-areas and the position of the first focal spot sub-area are very easy to define on the image, and will not affect the accuracy of the centroid detection. The selections of the intensity level of threshold and the size of detection windows

Table 1. Mean and standard deviation of the coordinates of centroids detected by auto-, averaging, thresholding and windowing algorithms from 36 images.

| | | Focal spot (0, 0) | | Focal spot (3, 3) | | Focal spot (5, 5) | | Overall | |
|--------|------|-------------------|-----------|-------------------|-----------|-------------------|-----------|-----------|-----------|
| | | X (pixel) | Y (pixel) | X (pixel) | Y (pixel) | X (pixel) | Y (pixel) | X (pixel) | Y (pixel) |
| Auto | Mean | 61.919 | 69.516 | 245.701 | 244.954 | 429.126 | 419.781 | — | — |
| | STD | 0.079 | 0.027 | 0.071 | 0.030 | 0.074 | 0.023 | 0.078 | 0.027 |
| Ave. | Mean | 49.111 | 48.337 | 239.156 | 237.077 | 428.901 | 424.161 | — | — |
| | STD | 0.012 | 0.745 | 0.018 | 0.864 | 0.010 | 1.025 | 0.015 | 0.876 |
| Thres. | Mean | 61.921 | 69.506 | 245.689 | 244.953 | 429.116 | 419.786 | — | — |
| | STD | 0.076 | 0.029 | 0.074 | 0.032 | 0.083 | 0.025 | 0.634 | 2.910 |
| Win. | Mean | 61.532 | 69.401 | 245.592 | 244.601 | 428.496 | 419.486 | — | — |
| | STD | 0.009 | 0.306 | 0.015 | 0.376 | 0.007 | 0.315 | 0.208 | 0.335 |

Table 2. Peak–valley values of the reconstructed sin wavefront with different patterns.

| Pattern | $\sin(0.03x)$ | $\sin(0.05x)$ | $\sin(0.03y)$ | $\sin(0.03y)$ |
|----------------------------|-----------------------|-----------------------|---------------|---------------|
| PV value (μm) | 0.326 | 0.351 | 0.346 | 0.376 |
| Pattern | $\sin(0.03x + 0.03y)$ | $\sin(0.05x + 0.05y)$ | Mean | STD |
| PV value (μm) | 0.365 | 0.350 | 0.3523 | 0.0171 |
| | | | | STD/mean |

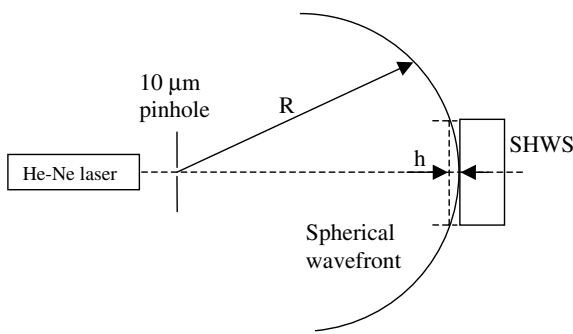


Figure 18. Verify the accuracy of the system by measuring the profile height of the spherical wavefront in the measurement field of the SHWS.

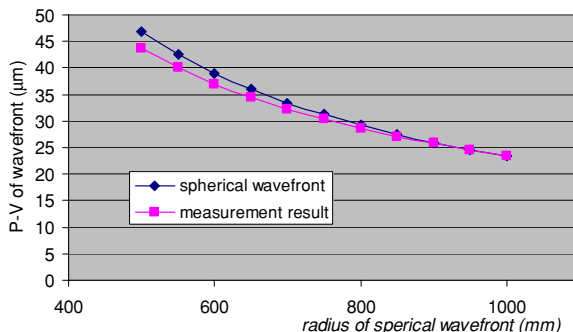


Figure 19. Ideal and measured profile heights of the spherical wavefront with different radii.

have significant influence on the detection accuracy of the spot centroid. However, the proposed centroid algorithm is certainly convergent for these two parameters and they can be determined easily in the software.

4. Wavefront reconstruction

The gradient of the wavefront can be calculated based on the motion of the centroid of the focal spot. In the SHWS, this

slope is determined by measuring the spatial displacement of the centroid as follows:

$$S_{ij}^x = \frac{\Delta x_{ij}}{f} \quad (4)$$

$$S_{ij}^y = \frac{\Delta y_{ij}}{f} \quad (5)$$

where S_{ij}^x is the average slope over a sub-aperture diameter in the X direction; S_{ij}^y is the average slope over a sub-aperture diameter in the Y direction; Δx_{ij} is the displacement of a measurement spot centroid from the reference spot centroid in the X direction; Δy_{ij} is the displacement of a measurement spot centroid from the reference spot centroid in the Y direction; f is the focal length of the lenslet array, as shown in figure 13.

Once the local wavefront slopes have been determined, the wavefront can be reconstructed by performing a type of integration on the slope measurements. The two primary types of wavefront reconstruction methods are zonal and modal. The zonal wavefront reconstruction is a type of numerical integration. The modal wavefront reconstruction fits the data to a set of orthogonal surface polynomials. In our system, the Southwell zonal reconstruction [23] and Zernike modal reconstruction [24] methods are applied. Our software system can automatically calculate the slopes and reconstruct the wavefront by the Southwell zonal or Zernike modal method, as shown in figure 14.

5. Study on accuracy of the system

5.1. Measurement of sine wavefront

Many experiments have been conducted to verify the accuracy and repeatability of our wavefront sensing system. In this experiment, we use one SLM to generate various wavefront patterns and use another SLM as the digital SHWS to measure the wavefront. Figure 15 shows some sine wavefront patterns generated by the SLM. Figure 15(a) has

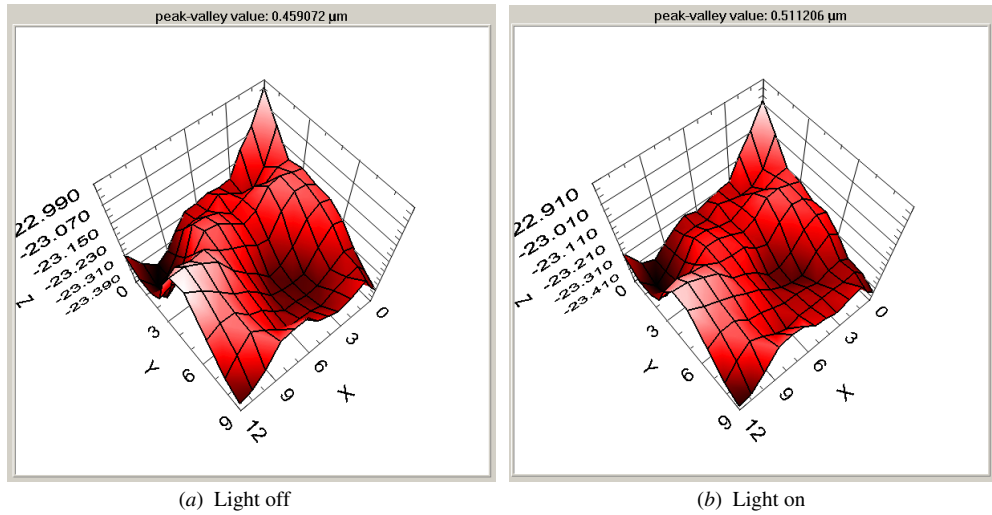


Figure 20. Profiles of the wavefront reflected by the mirror surface measured when (a) the light is off; (b) the light is on.

Table 3. Ideal and measured profile heights of the spherical wavefront with different radii in the measurement field of the SHWS.

| Radius (mm) | h_{ideal} (μm) | h_{meas} (μm) | Δh (μm) | $\Delta h\%$ |
|-------------|--------------------------------------|-------------------------------------|------------------------------|--------------|
| 500 | 46.815 | 43.605 | -3.21 | -6.86% |
| 550 | 42.559 | 40.069 | -2.49 | -5.85% |
| 600 | 39.012 | 36.987 | -2.025 | -5.19% |
| 650 | 36.011 | 34.543 | -1.468 | -4.08% |
| 700 | 33.439 | 32.248 | -1.191 | -3.56% |
| 750 | 31.209 | 30.459 | -0.75 | -2.40% |
| 800 | 29.259 | 28.695 | -0.564 | -1.93% |
| 850 | 27.537 | 27.088 | -0.449 | -1.63% |
| 900 | 26.007 | 25.795 | -0.212 | -0.82% |
| 950 | 24.638 | 24.542 | -0.096 | -0.39% |
| 1000 | 23.407 | 23.409 | 0.002 | 0.01% |

Table 4. Peak–valley values of the wavefront reflected by a mirror surface which is measured when the light is on and off, respectively.

| Time | PV value (μm) | |
|----------|----------------------------|----------|
| | Light off | Light on |
| 1 | 0.459 | 0.511 |
| 2 | 0.504 | 0.482 |
| 3 | 0.494 | 0.458 |
| 4 | 0.498 | 0.490 |
| 5 | 0.523 | 0.525 |
| 6 | 0.504 | 0.531 |
| 7 | 0.498 | 0.478 |
| 8 | 0.492 | 0.499 |
| 9 | 0.499 | 0.506 |
| 10 | 0.496 | 0.474 |
| Mean | 0.4967 | 0.4954 |
| STD | 0.0159 | 0.0232 |
| STD/mean | 3.20% | 4.68% |

the pattern of $A \sin(bx)$, and figure 15(b) has the pattern of $A \sin(bx + cy)$.

In this experiment, the pitch of the lenslet array is 1.28 mm, the focal length of the lenslet is 100 mm and the wavelength is 633 nm. A CMOS camera is used to detect the spot images. The resolution of the CMOS is 1280 ×

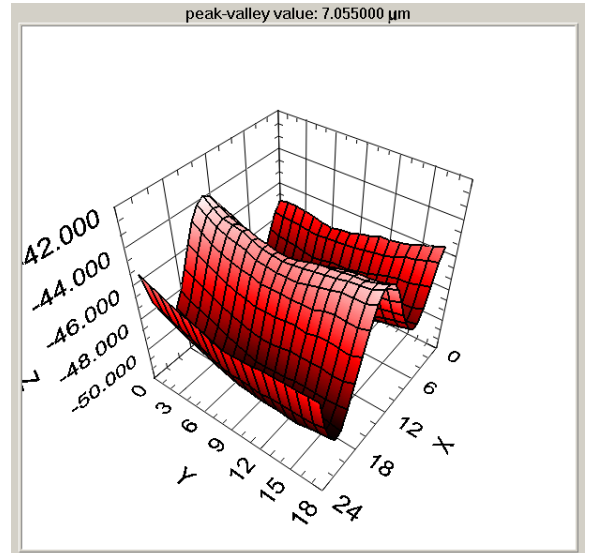


Figure 21. Profile of the wavefront reflected by a real part surface.

1024, and the pixel size is 12 μm . Figure 16(a) shows one of the spot images generated by the digital SHWS. The effect of diffraction in the image is very strong. It is difficult for common centroid algorithms to correctly detect the centroids in the image. However, our algorithm can detect all the centroids in the image accurately, as shown in figure 16(b).

The Southwell zonal reconstruction method is used for this and all the following experiments. Figure 17 shows some 3D profiles of the reconstructed wavefront. They have the patterns of $\sin(0.03x)$, $\sin(0.05x)$, $\sin(0.03y)$, $\sin(0.05y)$, $\sin(0.03x+0.03y)$ and $\sin(0.05x+0.05y)$, respectively. The peak–valley (PV) value of each wavefront is shown in table 2. The mean of the PV values is 0.352 μm , and the standard deviation is 0.017 μm .

From the measurement results, we can see that the measured wavefront coincides with the defined sine wavefront well, and the PV values of the measured wavefront are also very stable even if the patterns of the wavefront are changed.

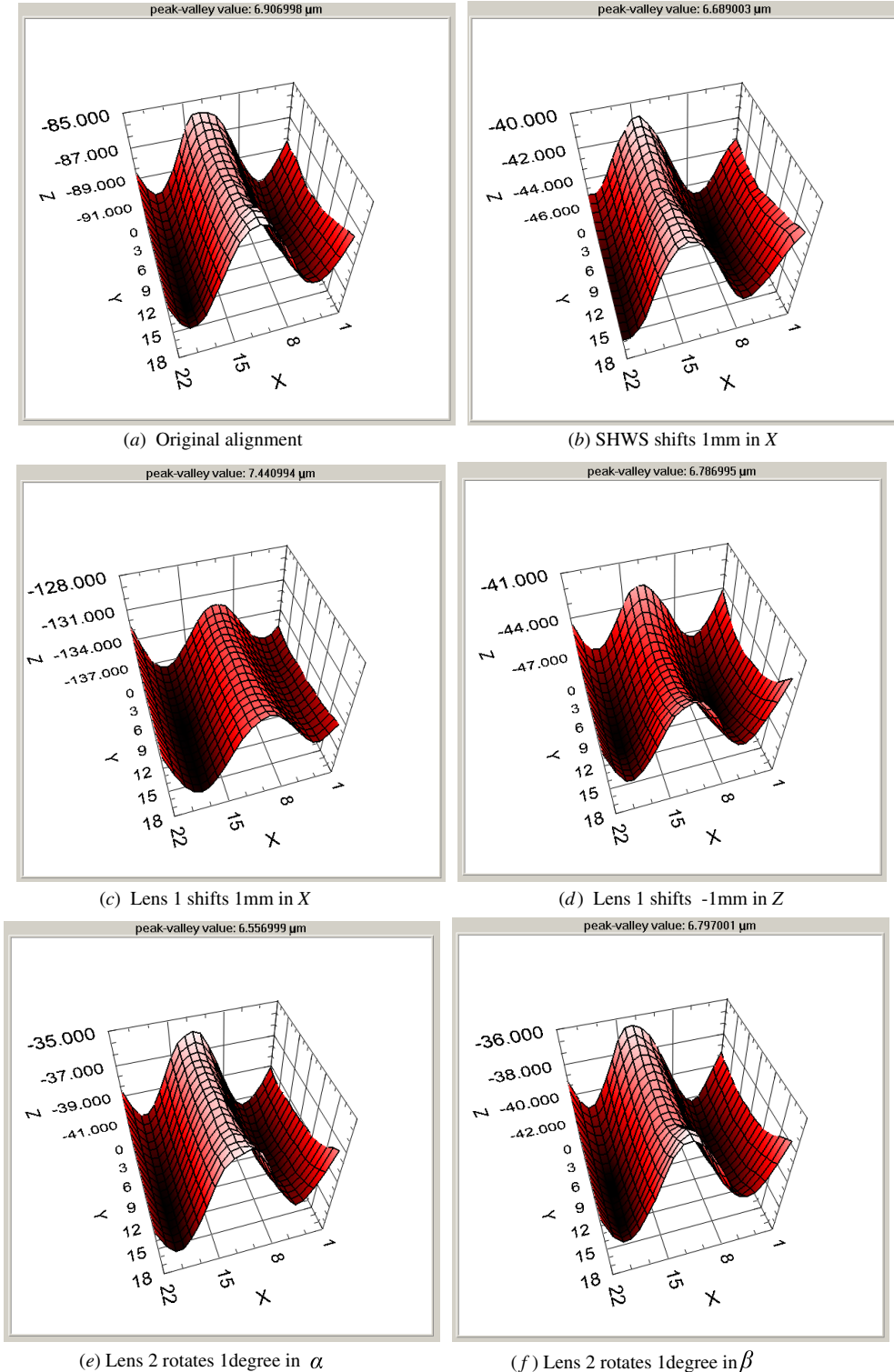
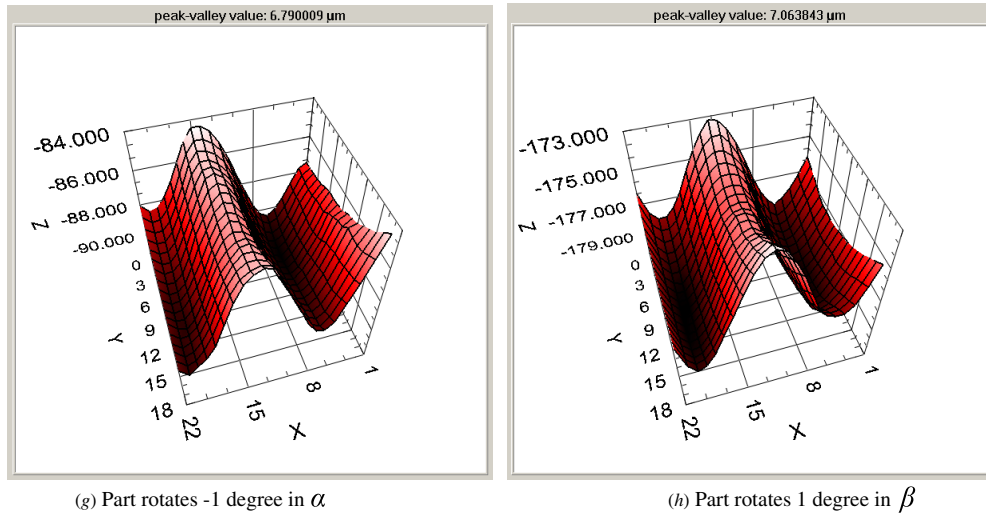


Figure 22. Study of the influence of misalignment of optical components on the accuracy of the surface measurement: (a) original alignment; (b) SHWS shifts 1 mm in the X direction; (c) lens 1 shifts 1 mm in the X direction; (d) lens 1 shifts -1 mm in the Z direction; (e) lens 2 rotates 1° in the α direction; (f) lens 2 rotates 1° in the β direction; (g) part rotates -1° in the α direction; (h) part rotates 1° in the β direction.

5.2. Measurement of spherical wavefront

We also use a spherical wavefront to verify the accuracy of our system. The spherical wavefront is generated with a point light source as shown in figure 18. We put the SHWS at different

distances from the pinhole to get the spherical wavefront with different radii. Then we calculate the profile heights h of the ideal wavefront in the measurement field of the SHWS and compare with measurement results. Table 3 shows the ideal profile heights h_{ideal} and measured profile heights h_{meas}

**Figure 22.** (Continued.)**Table 5.** Peak–valley values of the wavefront reflected by a real part surface.

| Time | 1 | 2 | 3 | 4 | 5 | Mean | STD | STD/mean |
|----------------------------|-------|-------|-------|-------|-------|--------|--------|----------|
| PV value (μm) | 7.055 | 7.040 | 7.027 | 7.047 | 7.016 | 7.0370 | 0.0156 | 0.22% |

Table 6. Peak–valley values of the wavefront with misalignment of optical components.

| Misalignment | PV value (μm) |
|--------------------------------------|----------------------------|
| Original alignment | 6.907 |
| SHWS shifts 1 mm in X | 6.689 |
| Lens 1 shifts 1 mm in X | 7.441 |
| Lens 1 shifts -1 mm in Z | 6.787 |
| Lens 2 rotates 1° in α | 6.557 |
| Lens 2 rotates 1° in β | 6.797 |
| Part rotates -1° in α | 6.790 |
| Part rotates 1° in β | 7.064 |
| Mean | 6.879 |
| STD | 0.2709 |
| STD/mean | 3.94% |

as well as the differences between them. Figure 19 shows the figures of the ideal and measured profile heights of the spherical wavefront versus radii.

We can see that the measurement accuracy of the system is quite high. It can be up to 2 nm when the radius of the spherical wavefront is 1000 mm. However, a systematic error can be found in the system. The variance between the theoretical and measured data increases with the decrease of the radius of the wavefront. The error is mainly caused by the reference image. We use a collimated beam to generate a super-plane surface as the reference. This beam may not be well collimated, and there is a spherical component in the beam. So high precise components should be used for system alignment and calibration.

6. Study on repeatability of the system

6.1. Measurement of mirror surface

We have conducted several groups of repeatability experiments using two mirrors. One mirror is used as the target object, and the other is used as the reference. We took ten spot images in every group of experiments, one image per 10 min. The light of the lab is on for one group of experiments, and it is off for another group of experiments.

Figure 20 shows some 3D profiles of the reconstructed wavefront reflected by the mirror surface. Figure 20(a) shows a profile of the wavefront measured when the lab light is on. Figure 20(b) shows a profile of the wavefront measured when the lab light is off. Table 4 gives the PV values, means and standard deviations of the measurements when the lab light is on and off, respectively.

The experimental results demonstrate that the repeatability of the system is quite good. The standard deviation of the measurements is within 16 nm when the lab light is off. When the lab light is on, the standard deviation becomes a little bit higher, up to 23 nm. But generally speaking, the lighting condition of the environment does not influence the accuracy of the measurement significantly.

6.2. Measurement of real part surface

We also conducted a repeatability experiment using a real part fabricated by a five-axis precision machine. The section curve of the original design of the part is a polynomial with

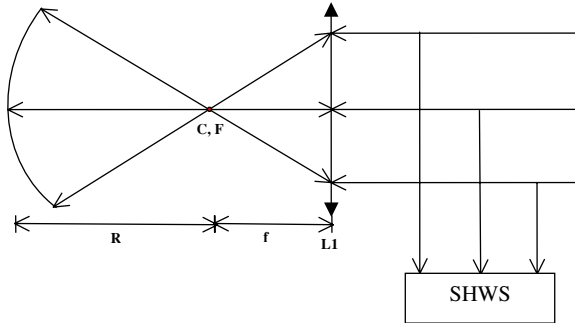


Figure 23. Optical setup for aspherical surface measurement.

power 10, defined by the following formula:

$$\begin{aligned} y = & 0.008 - 0.000\,226\,86x + 3.0905 \times 10^{-6}x^4 \\ & - 1.509 \times 10^{-8}x^6 + 2.9747 \times 10^{-11}x^8 \\ & - 2.0204 \times 10^{-14}x^{10}. \end{aligned} \quad (6)$$

In this experiment, the pitch of the lenslet array is 0.622 mm, the focal length of the lenslet is 21.2 mm and the wavelength is 633 nm. The same CMOS camera with the resolution of 1280×1024 is used to detect spot images. We use a mirror as the reference and measure the part five times in one day. Figure 21 shows the profile of the measured wavefront, and table 5 shows the PV values, means and standard deviations of the measurements. The standard deviation of the measurements is still within 16 nm. It is coincident with the measurement of the mirror surface.

7. Study on sensitivity of the system to misalignment

In the SHWS system, since the measurement wavefront goes through the same optical system as the reference wavefront, the errors caused by physical defects of optical elements can be eliminated. So the SHWS has good immunity to optical imperfection such as misalignment of the optical system. In this experiment, we study the influence of misalignment of optical components on the accuracy of the measurement.

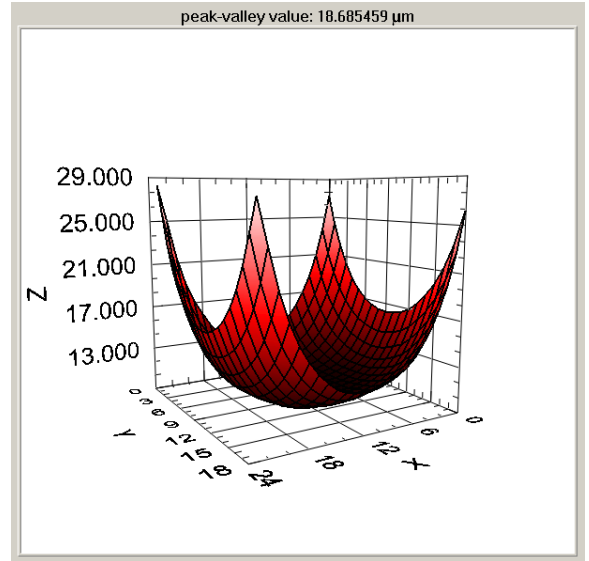


Figure 24. Profile of the wavefront reflected by a real aspherical surface.

The same part used in the repeatability experiment is used for this experiment. We shift and rotate the lens, the SHWS as well as the part, and measure the surface profile of the part using our system. Figure 22 shows some surface profiles of the wavefront for some misalignment cases. For example, figure 22(a) shows the profile of the wavefront at the original alignment position. In figure 22(b), the SHWS is shifted 1 mm in the X direction. In figures 22(c) and (d), lens 1 of the $2f+2f$ optical system is shifted 1 mm and -1 mm in the X and Z directions, respectively. In figures 22(e) and (f), lens 2 is rotated 1° in the α and β directions, respectively. In figure 22(g), the part is rotated -1° in the α direction, and the part is rotated 1° in the β direction in figure 22(h). The shift and rotate directions are the same as illustrated in figure 3. The PV value of the wavefront in each case is shown in table 6.

From the experimental results, we can see that the measurement fields are changed when some misalignments

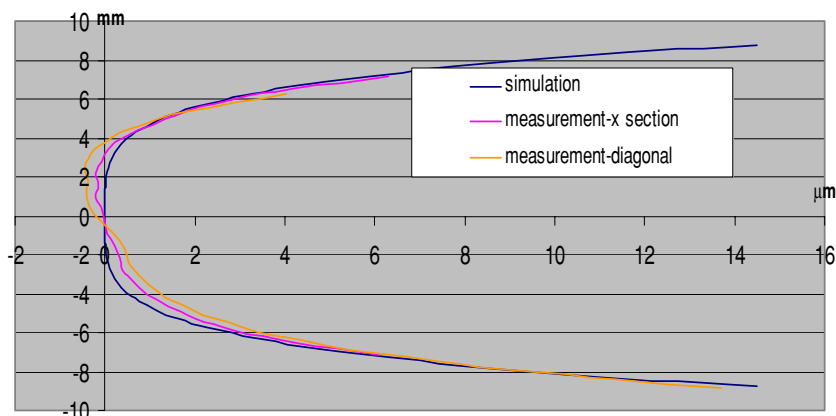


Figure 25. Compare the measured wavefront reflected by the aspherical surface with the propagated wavefront simulated by the wavefront tracing platform.

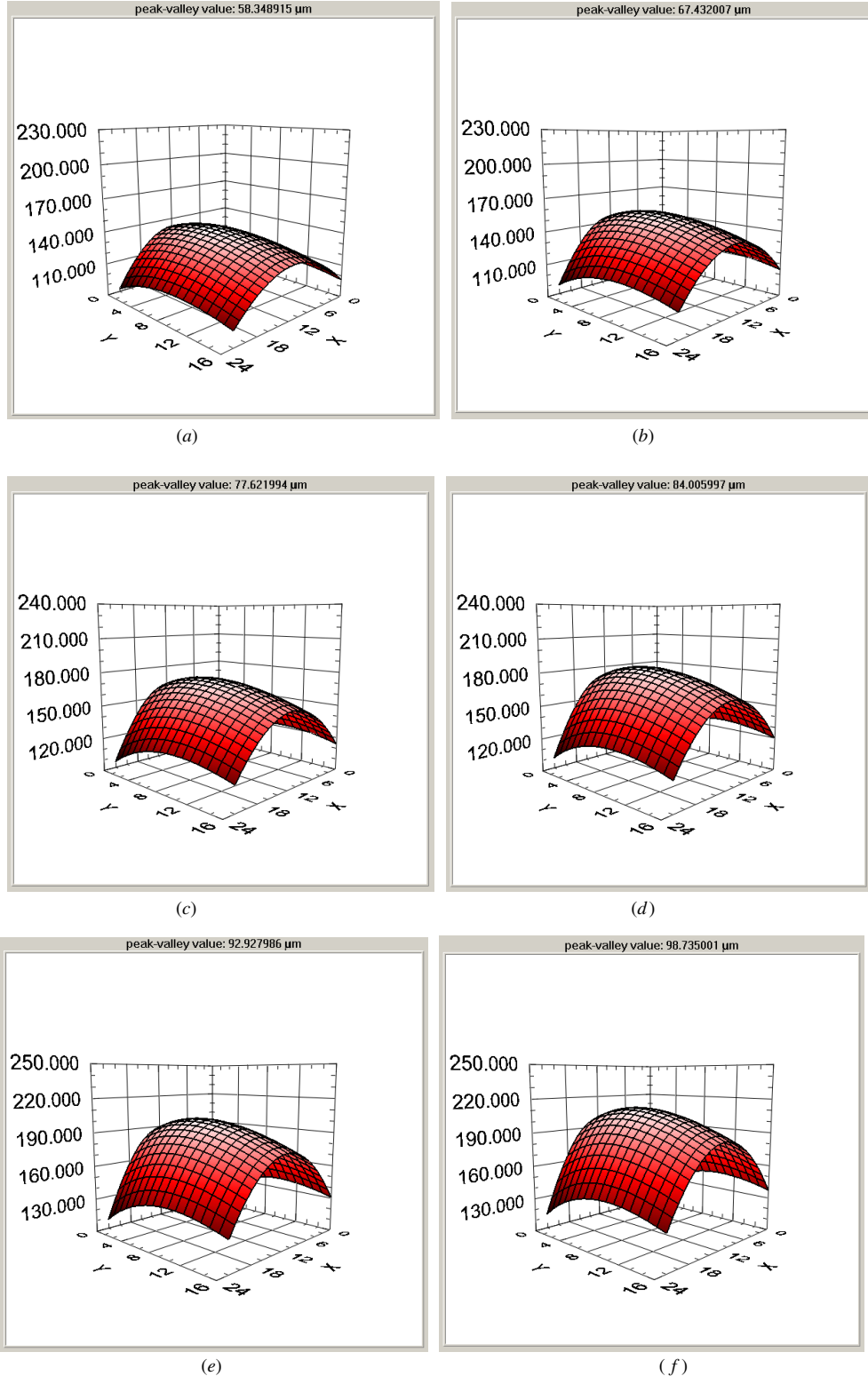


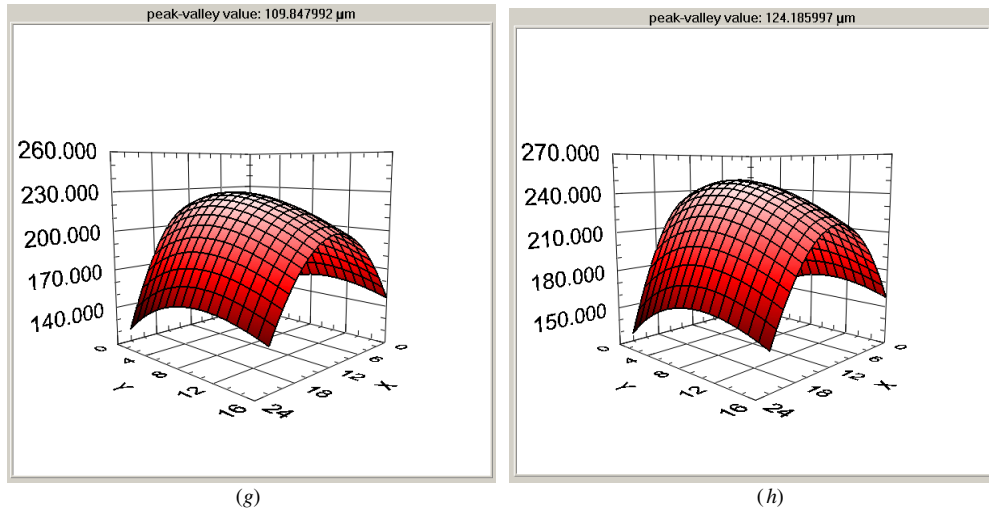
Figure 26. Monitoring and measuring the deformation of a wafer surface in real time.

happen. However, the PV values of the wavefront are not changed significantly. The standard deviation of the measurements with misalignment is still within $0.3 \mu\text{m}$. It demonstrates that our SHWS is immune to the misalignment of the system.

8. Measurement results of real surfaces

8.1. Measurement of aspherical surface

We have used our SHWS to measure some real surfaces. In this experiment, an aspherical surface fabricated by a diamond

**Figure 26.** (Continued.)

turning machine is measured. The aspherical surface is defined by the following formula:

$$Z = \frac{-6.25 \times 10^{-3}r^2}{1 + \sqrt{1 - 3.90625 \times 10^{-5}r^2}} - 9.6 \times 10^{-7}r^4. \quad (7)$$

A traditional spherical testing setup as shown in figure 23 is used for the aspherical surface measurement. The incident light is reflected by the designed aspherical surface and enters a collimating lens L1, so the spherical component of the wavefront is removed. Then the wavefront continues to propagate to the measurement plane of the SHWS. In this measurement, a spherical mirror with radius = 160 mm is used as the reference, and the reference surface has the following formula:

$$Z = 160 - \sqrt{160^2 - r^2}. \quad (8)$$

Figure 24 shows the 3D profile of the measured wavefront reflected from the real surface. We also used our software platform to simulate the ideal wavefront propagated from the designed surface and compare with the measurement results. Figure 25 shows the comparison of the propagated wavefront simulated by the wavefront tracing platform and the measured wavefront reflected by the real aspherical surface. The measurement results coincide with the simulation results very well.

8.2. Measurement of deformable surface

The SHWS is insensitive to vibration and noise, since focal spot images of the SHWS can be captured by a CCD or CMOS camera in a very short time. In addition, we have proposed an automatic centroid detection algorithm. This algorithm can automatically detect the centroid of the focal spot precisely and reliably by using an adaptive thresholding and dynamic windowing method, and the implementation of the algorithm is very fast. We have also developed a software system which can implement centroid detection, wavefront reconstruction automatically. So our digital SHWS system is applicable to on-line surface measurement.

In this experiment, the system is used to monitor and measure the profile of a deformable surface in real time, the surface of a raw wafer. Two opposite edges of the wafer are fixed, and a force is added at the center of the wafer to deform it gradually. We monitor the deformation of the wafer by measuring the surface profile of the wafer in real time. Some measurement results are shown in figure 26. Figure 26(a) shows the original position of the surface and the PV value of the measured wavefront at this position is 58.349 μm. From figures 26(b) to (h), the PV value of the wavefront changes to 67.432 μm, 77.622 μm, 84.006 μm, 92.928 μm, 98.735 μm, 109.848 μm and 124.186 μm, respectively. We can see that the deformation of the wafer surface is presented clearly by the system. In our system, the focal spot images can be taken and processed at a speed as high as 10 frames per second.

9. Conclusion

The Shack–Hartmann wavefront sensor provides a promising technology for non-contact surface measurement with a number of advantages over interferometry, such as large dynamic range, immunity to optical misalignment, insensitivity to vibration and noise, less complex and less expensive. The measurement accuracy of the SHWS is mainly dependent on the accuracy of the centroid detection of focal spots, since the SHWS splits the incident wavefront into many subsections and transfers the distorted wavefront detection into the centroid measurement.

In this paper, we have presented a new centroid measurement algorithm based on an adaptive thresholding and dynamic windowing method by utilizing image-processing techniques. The algorithm can detect the centroid of the focal spot accurately and robustly by eliminating the influence of various noises such as diffraction of the digital SHWS, unevenness and instability of the light source as well as deviation between the centroid of the focal spot and the center of the detection area.

Based on our automatic centroid detection method, we have built a digital SHWS system for surface profile

measurement. The focal length, size, pitch, format and layout of the lenslet array of digital SHWS can be changed flexibly according to requirements of different applications. We also have developed a software system which can automatically detect centroids of focal spots, reconstruct the wavefront and measure the profile of the surface.

We have studied the accuracy and repeatability of the system using various simulated and real surfaces. We also studied the influence of optical misalignment on the measurement accuracy by shifting and rotating the components of the optical system intentionally. The experimental results demonstrate that the accuracy and repeatability of the system are very good. The system is also immune to optical misalignment.

We have used our system to measure some real surfaces such as an aspherical surface. The measurement results coincide well with the simulation results obtained from the wavefront-tracing platform. Our system is also applicable to on-line surface measurement. We have used the system to monitor and measure the profile of a deformable surface in real time.

References

- [1] Forest C R, Canizares C R, Neal D R, McGuirk M and Schattenburg M L 2004 Metrology of thin transparent optics using Shack–Hartmann wavefront sensing *Opt. Eng.* **43** 742–53
- [2] Pfund J, Lindlein N and Schwider H 2001 Nonnull testing of rotationally symmetric aspheres: a systematic error assessment *Appl. Opt.* **40** 439–46
- [3] Bennett J M and Dancy J H 1981 Stylus profiling instrument for measuring statistical properties of smooth optical surfaces *Appl. Opt.* **20** 1785–802
- [4] Bennett J M 1976 Measurement of the rms roughness, autocovariance function and other statistical properties of optical surfaces using a FECO scanning interferometer *Appl. Opt.* **15** 2705–21
- [5] Francon F and Mallick S 1971 *Polarization Interferometers: Applications in Microscopy and Macroscopy* (New York: Wiley-Interscience)
- [6] Koliopoulos C L 1981 Interferometric optical phase measurement techniques *PhD dissertation* University of Arizona
- [7] Wyant J C, Koliopoulos C L, Bhushan B and George O E 1984 An optical profilometer for surface characterization of magnetic media *ASLE Trans.* **27** 101–13
- [8] Koch J A et al 2001 Experimental comparison of a Shack–Hartmann sensor and a phase-shifting interferometer for large-optical metrology applications *Appl. Opt.* **39** 4540–6
- [9] Pfund J, Lindlein N and Schwider H 1998 Absolute sphericity measurement: a comparative study of the use of interferometry and a Shack–Hartmann sensor *Opt. Lett.* **23** 742–4
- [10] Greivenkamp J E and Smith D G 2008 Graphical approach to Shack–Hartmann lenslet array design *Opt. Eng.* **47**
- [11] Li X, Zhao L P, Fang Z P, Asundi A and Yin X M Surface measurement with Shack–Hartmann wavefront sensing technology *Proc. 9th Int. Symp. on Laser Metrology (Singapore, 30 June–2 July 2008)*
- [12] Zhao L P, Bai N, Li X, Ong L S, Fang Z P and Asundi A K 2006 Efficient implementation of SLM as diffractive optical microlens array in digital Shack–Hartmann wavefront sensor *Appl. Opt.* **45** 90–4
- [13] Cao G and Yu X 1994 Accuracy analysis of a Hartmann–Shack wavefront sensor operated with a faint object *Opt. Eng.* **33** 2332–5
- [14] Irwan R and Lane R G 1999 Analysis of optimal centroid estimation applied to Shack–Hartmann sensing *Appl. Opt.* **38** 6737–43
- [15] Zhang A, Rao C, Zhang Y and Jiang W 2004 Sampling error analysis of Shack–Hartmann wavefront sensor with variable subaperture pixels *J. Mod. Opt.* **51** 2267–78
- [16] Park S K and Baik S H 2002 A study on a fast measuring technique of wavefront using a Shack–Hartmann sensor *Opt. Laser Technol.* **34** 687–4
- [17] Ren J F, Rao C H and Li Q M 2002 An adaptive threshold selection method for Hartmann–Shack wavefront sensor *Opt. Electron. Eng.* **29** 1–5
- [18] Baik S H, Park S K, Kim C J and Cha B 2007 A center detection algorithm for Shack–Hartmann sensor *Opt. Laser Technol.* **39** 262–7
- [19] Arulmozhivarman P, Kumar L Praveen and Ganesan A R 2006 Measurement of moments for centroid estimation in Shack–Hartmann wavefront sensor—a wavelet-based approach and comparison with other methods *Optik* **117** 82–7
- [20] Poyneer L A, Palmer D W, LaFortune K N and Bauman B 2005 Experimental results for correlation-based wave-front sensing *Proc. SPIE* **5894** 207–20
- [21] Prieto P M, Vargas-Martin F, Goelz S and Artal P 2000 Analysis of the performance of the Hartmann–Shack sensor in the human eye *J. Opt. Soc. Am. A* **17** 1388–98
- [22] Baker K L and Moallem M M 2007 Iteratively weighted centroiding for Shack–Hartmann wave-front sensors *Opt. Exp.* **15** 5147–59
- [23] Southwell W H 1980 Wave-front estimation from wave-front slope measurements *J. Opt. Soc. Am.* **70** 998–1006
- [24] Dai G M 1996 Modal wave-front reconstruction with Zernike polynomials and Karhunen–Loeve functions *J. Opt. Soc. Am. A* **13** 1218–25